Aspects of Ptychographic Scanning-TEM:

1. **Efficient Phase Contrast Imaging via Electron Ptychography, a Tutorial** *(T.J. Pennycook)*
2. **Phase Imaging beyond the Diffraction Limit with Electron Ptychography** *(David A. Muller)*
3. **Imaging Low Z Materials in Crystalline Environments Via Scanning Transmission Electron Microscopy** *(Scott D. Findlay)*
4. **Advances in STEM and EELS: New Operation Modes, Detectors and Software** *(Ondrej Krivanek)*

doi:10.1017/S1431927619014156
Microsc. Microanal. 25 (Suppl 2), 2019

Efficient Phase Contrast Imaging via Electron Ptychography, a Tutorial

Timothy J. Pennycook[1,2,*], Gerardo T. Martinez[3], Colum M. O'Leary[3], Hao Yang[4], Peter D. Nellist[3]

[1.] Electron microscopy for materials science, University of Antwerp, Antwerp, Belgium.
[2.] Stuttgart Center for Electron Microscopy, Max Planck Institute for Solid State Research, Stuttgart Germany.
[3.] Department of Materials, University of Oxford, Oxford, UK.
[4.] Molecular Foundry, Lawrence Berkeley National Laboratory, USA
* Corresponding author: tim.pennycook@uantwerpen.be

As electron optics continue to improve, damage from the electron beam ever increasingly places the limits on the ability of electron microscopy to reveal the properties of materials at atomic resolution. Although originally developed for extending resolution beyond the diffraction limit, electron ptychography has recently been adapted to maximize the efficiency at which imaging can be performed in scanning transmission electron microscopy (STEM). In this tutorial the underlying principles of ptychography, its performance relative to other techniques and practical aspects of its application will be discussed.

Ptychography is a phase contrast imaging technique. However, unlike phase contrast imaging in high-resolution transmission electron microscopy (HRTEM), it requires neither a physical phase plate or the use of lens aberrations to form contrast. Instead, during the STEM scan, the details of the convergent beam electron diffraction (CBED) patterns are recorded with a pixelated detector as a function of probe position. The so called phase problem is solved via the mutual interference of the diffracted CBED disks with the undiffracted bright field (BF) disk. This interference of many overlapping beams is untangled by performing the Fourier transform with respect to probe position. This allows the phase and amplitude of the interference of each diffracted disk with the BF disk to be determined individually. The phase and amplitude of all spatial frequencies can then be determined with the common reference to their interference with the BF disk. A phase image is then constructed by interfering all the spatial frequencies with the inverse Fourier transform.

By determining the phase and amplitude of each spatial frequency separately and averaging across the entire region of disk overlap where signal transfer occurs one maximizes the amount of signal acquired. At the same time, by excluding regions where the transfer of a given spatial frequency do not occur, one minimizes the amount of noise. Thus such forms of ptychography, which include the single side band (SSB) [1] and Wigner distribution deconvolution (WDD) [2] methods, can maximize the signal to noise ratio, resulting in greater dose efficiency in comparison to STEM methods that use fixed integration regions such as BF, annular bright field (ABF), and differential phase contrast (DPC).

STEM ptychography can also outperform the dose efficiency of phase contrast imaging in HRTEM, currently the method of choice for imaging the most delicate materials, for instance in cryo electron microscopy. STEM ptychography is much more robust to partial temporal coherence than HRTEM. This is because of the presence of achromatic lines in the in the double disk overlap regions in probe reciprocal space [4]. In addition because the contrast transfer function for ptychography extends out to twice the convergence angle defined by the probe forming aperture SSB and WDD ptychography have intrinsic double resolution in comparison to HRTEM for which the resolution is limited by angle defined

by the aperture itself.

Especially for in focus probe ptychography, necessary for obtaining simultaneous annular dark field (ADF) images, one desires fast efficient detectors to capture the 4D datasets. This is especially true if one wishes to reach low doses, as the dwell time cannot be faster than the time resolution of the camera. Fortunately, ptychography requires relatively few pixels in the CBED images [3] allowing to gain speed by using small chips or binning, and current options for efficient direct electron detectors will be discussed.

The original SSB code has evolved into ptychoSTEM, a free and open source MATLAB based package for performing ptychography. An introduction to ptychoSTEM will be given, including examples of processing data. An additional benefit of ptychography is that one can correct for residual aberrations after taking the data. This means one can save dose by avoiding careful fine tuning of the imaging conditions. It can also be important for correctly interpreting the phase, for instance when looking for subtle changes in contrast due to charge transfer. In addition one can intentionally add in defocus to perform optical sectioning from a single scan, providing substantial dose savings in comparison to the usual many scans at different focuses.

References:

[1] T. J. Pennycook *et al*., Ultramicrosopy **151** (2015)**,** p. 160.
[2] H. Yang et al., Nat. Commun. **7** (2016), p. 12532.
[3] H. Yang, T. J. Pennycook., and P. D. Nellist, Ultramicrosopy **151** (2015)**,** p. 252.
[4] T. J. Pennycook *et al.*, Ultramicroscopy **196** (2019), p. 131.
[5] TJP acknowledges support from the EU Marie Skłodowska-Curie grant No. 655760 – DIGIPHASE, and the European Research Council Grant no. 802123 HDEM.

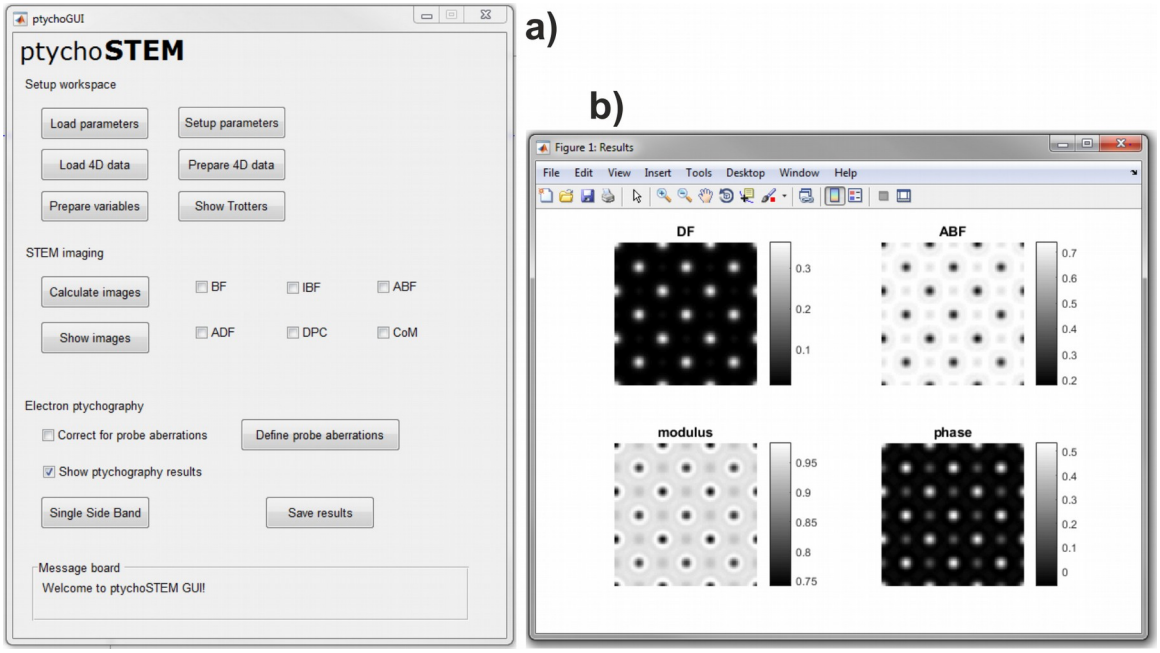

Figure 1. a) The ptychoSTEM graphical user interface. b) The program can compute various imaging modes from the 4D datasets for comparison, in this case from data simulated using [100] $SrTiO_3$.

doi:10.1017/S143192761900076X
Microsc. Microanal. 25 (Suppl 2), 2019

Phase Imaging beyond the Diffraction Limit with Electron Ptychography

David A. Muller[1,4,*], Zhen Chen[1], Yi Jiang[2], Michal Odstrcil[3], Yimo Han[1], Prafull Purohit[2], Mark W. Tate[2], Sol M. Gruner[2,4], Veit Elser[2]

[1.] School of Applied and Engineering Physics, Cornell University, Ithaca, NY 14853, USA
[2.] Department of Physics, Cornell University, Ithaca, NY 14853, USA
[3.] Paul Scherrer Institut, CH-5232 Villigen PSI, Switzerland
[4.] Kavli Institute at Cornell for Nanoscale Science, Ithaca, NY 14853, USA
* Corresponding author: David.a.Muller@cornell.edu

The past three decades have seen the rapid development and maturation of aberration-corrected electron lenses. With the recent advances in detector technology and reconstruction algorithms, the resolution limits are now dominated by counting noise through the maximum allowable dose, either by radiation damage to the sample, or by recording times. Ptychographic phase retrieval algorithms offer an approach to using all of the scattered electrons – potentially enhancing both the resolution and dose-efficiency. Here we show how in-focus ptychography enables imaging at more than double the diffraction limit of the lens, and how out-of-focus ptychography improves the dose efficiency compared with ADF STEM, simultaneously providing a four times faster acquisition, double the information limit and double the precision.

Image resolution is dominated by the energy (or wavelength) of the electron beam and the quality of the lens. Two-dimensional materials are imaged with low beam energies to avoid damaging the samples, limiting spatial resolution to ~1 Å. By combining our new design of electron microscope pixel array detector (EMPAD) [1] which has the dynamic range to record the complete distribution of transmitted electrons at every beam position, and a ptychographic phase retrieval algorithm [2] to process the data, we have been able to increase the spatial resolution well beyond the traditional lens limitations reaching a 0.39 Å resolution for MoS_2, at 80 keV, the same dose and imaging conditions where conventional imaging modes reach only 0.98 Å [3]. The improved resolution, dose efficiency and robustness to environmental noise enabled by ptychography make it easy to identify defects such as sulfur monovacancies, as well as subtle structural arrangements and tilts on the sulfur sublattice that are undetectable by conventional imaging modes. For twisted bilayers we are able to resolve the shear distortions and interactions between the layers (Figure 1). [3]

In-focus ptychography, like conventional STEM, is not well suited to imaging large areas at high spatial resolution – as the resolution is increased, the number of samples required grows quadratically in dwell time or dose. Operating out-of-focus decouples the resolution and real-space sampling requirements [4], provided the detector has sufficient dynamic range and pixels. While simulations have shown the out-of-focus reconstructions to have better convergence at low dose, compare to in-focus [3], in practice this was not the case when simple initial probe estimates were used. With improved probe diversity, we have been able to image 120 nm fields of view with 0.69 Å resolution at 80 keV producing 6000x6000 pixel images. Figure 2 shows the dose dependence and resolution of out-of-focus ptychography on WS_2 monolayers. Figure 2d shows the precision with which we can measure S-S or W-W bond lengths, both in ptychography and ADF STEM, showing a roughly factor of two advantage for ptychography over ADF at the same dose.[5]

References:

[1] MW Tate, *et al*, Microscopy and Microanalysis **22** (2016), p. 237.
[2] A Maiden, *et al*, Ultramicroscopy 109 (2009), p. 1256.
[3] Y. Jiang *et al*, Nature **559**, (2018), p343.
[4] C. S. Allen, *et al*,. Microscopy and Microanalysis, **24(S1)**, (2018) p. 186–187.
[5] We thank Jiwoong Park, Saien Xie, Hui Gao, Ming-Hui Chiu, and Lain-Jong Li for samples. Research supported by US National Science Foundation (grants DMR-1539918, DMR-1429155, DMR-1719875) & US Department of Energy Basic Energy Sciences (DE-SC0005827).

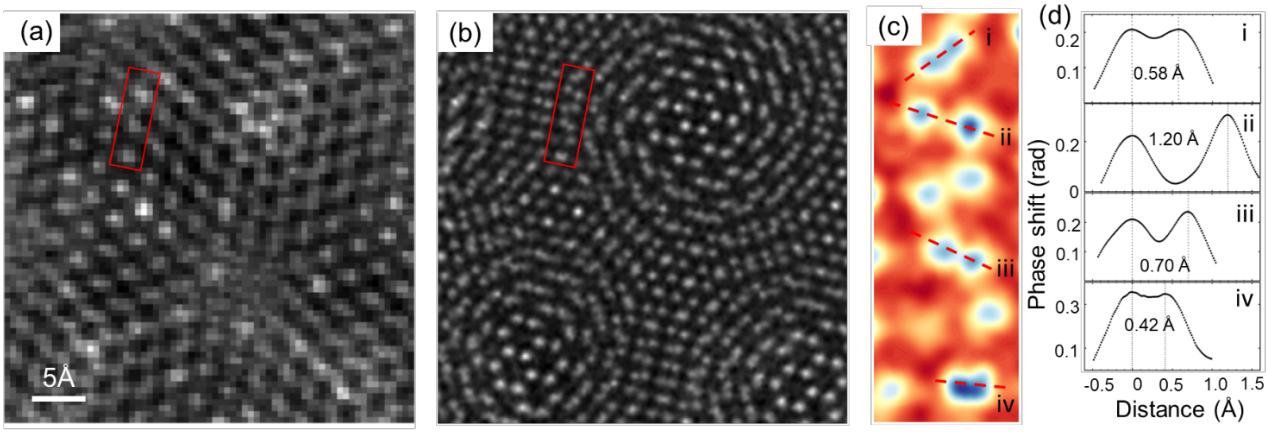

Figure 1. Real space resolution demonstration of full-field, in-focus ptychography using a twisted bilayer MoS_2. (a) Synthesized ADF image; (b) Phase image from ptychographic reconstruction; (c) Enlarged phase image of the marked area in (b); (d) Intensity line profile of corresponding positions labeled with dashed red lines in (c). The peak separation distances are overlaid on (d). Data adapted from [3]

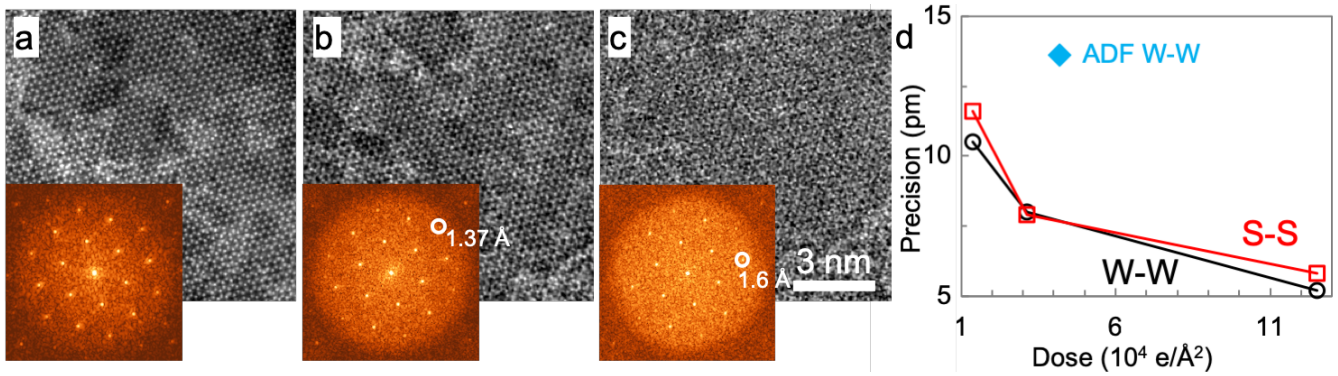

Figure 2. Dose-dependence of out-of-focus Ptychographic reconstructions of a monolayer WS_2 sample: a. 58000 e/Å^2; b. 3300 e/Å^2; c. 790 e/Å^2. These are extracts from a larger field of view. Scan step size is 0.85 Å. The dose-dependence of the precision with which the W-W and S-S bond lengths can be measured from pychography, and ADF imaging (only W-W was measurable at low dose) is shown in (d).

doi:10.1017/S1431927619009395
Microsc. Microanal. 25 (Suppl 2), 2019

Imaging Low Z Materials in Crystalline Environments Via Scanning Transmission Electron Microscopy

SD Findlay[1*], N Shibata[2], Y Ikuhara[2], L Clark[3], HG Brown[4], TC Petersen[1], DM Paganin[1] and MJ Morgan[1]

[1.] School of Physics and Astronomy, Monash University, Melbourne, Australia
[2.] Institute of Engineering Innovation, The University of Tokyo, Tokyo, Japan
[3.] School of Physics and Astronomy, University of Glasgow, Glasgow, UK
[4.] National Centre for Electron Microscopy, Lawrence Berkeley National Laboratory, Berkeley, USA
* Corresponding author: scott.findlay@monash.edu

Amongst atomic-resolution scanning transmission electron microscopy (STEM) imaging modes, annular dark-field (ADF; shown schematically in Fig. 1(a)) is particularly popular since it produces directly interpretable images – with bright peaks indicating atomic columns – over a wide thickness range and is fairly robust against aberrations. The thickness-defocus tableaus of ADF images in Fig. 1(b) for $SrTiO_3$ and Fig. 1(c) for Al_3Li are consistent with this. That ADF peak intensities scale roughly as the atomic number (Z) squared helps distinguish elements but also means low Z element columns may not be visible when high Z element columns are nearby – the O columns in Fig. 1(b) and Li columns in Fig. 1(c) are not visible – necessitating other methods to identify low Z element columns. This talk with review some atomic-resolution STEM imaging modes better suited to observing low Z element columns.

A decade ago it was found that so-called annular bright field (ABF) imaging, which uses an annular detector spanning the outer portion of the bright field disk, also produces directly interpretable images – with dark troughs indicating atomic columns – over a wide thickness range [1,2]. Moreover, the atomic number dependence is relatively weak and so both low and high Z element columns are visible simultaneously. The thickness-defocus tableaus of ABF images in Figs. 1(b) and (c) are consistent with this. ABF has since found many applications, including probing oxygen octahedra rotation in perovskites and charging/discharging in lithium battery materials. Further improvements have been suggested, such as so-called enhanced ABF (eABF) imaging [3] shown in the thickness-defocus tableaus in Figs. 1(b) and (c), and also more case-specific optimisations [4]. We overview some guiding principles and limitations of ABF imaging and its variants for imaging low Z elements.

Recent developments in fast-readout pixel array detectors allow not only more scope for synthesizing optimal annular detector configurations [4] but also for new imaging modes. In particular, differential phase contrast (DPC) [5,6] and ptychography [7-9] methods allow good imaging of low Z element columns and are dose-efficient [6,8]. The thickness-defocus tableaus of phase reconstructions – integrated DPC (iDPC) images in the parlance of Ref. [6] – in Figs. 1(b) and (c) are consistent with this. DPC and ptychography yield quantitative reconstructions of the projected electrostatic potential when the phase object approximation holds, but this breaks down for crystals thicker than a few nanometers when using atomically-fine electron probes [10,11]. The thickness-defocus tableaus of iDPC images in Fig. 1(b) and (c) shows this breakdown once it is appreciated that the true projected electrostatic potential should increase linearly with thickness. Specifically, in the iDPC images around zero relative defocus (relative to the sample midplane, the conditions seemingly most favourable for DPC STEM [10]) the iDPC signal only increases for the first 50–100 Å. We overview some approaches and limitations to DPC imaging and other phase contrast imaging modes for imaging low Z elements [12].

References:

[1] E Okunishi et al., Microsc Microanal **15(Suppl 2)** (2009), p. 164.
[2] SD Findlay et al., Ultramicroscopy **110** (2010), p. 903.
[3] SD Findlay et al., Ultramicroscopy **136** (2014), p. 31.
[4] J Gonnissen et al., Applied Physics Letters **105** (2014), p. 063116.
[5] K Müller et al., Nature Communications **5** (2014), p. 5653.
[6] I Lazić, EGT Bosch, S Lazar, Ultramicroscopy **160** (2016,) p. 265.
[7] CT Putkunz et al., Physical Review Letters **108** (2012), p. 073901.
[8] H Yang et al., Nature Communications **7** (2016), p. 12532.
[9] Y Jiang et al., Nature **559** (2018), p. 343.
[10] R Close et al., Ultramicroscopy **159** (2015,) p. 124.
[11] K Müller-Caspary et al., Ultramicroscopy **178** (2017), p. 62.
[12] This research was supported under the Australian Research Council Discovery Projects funding scheme (Project No. DP160102338). We thank all our collaborators who have contributed so much to the various pieces of research overviewed in this talk.

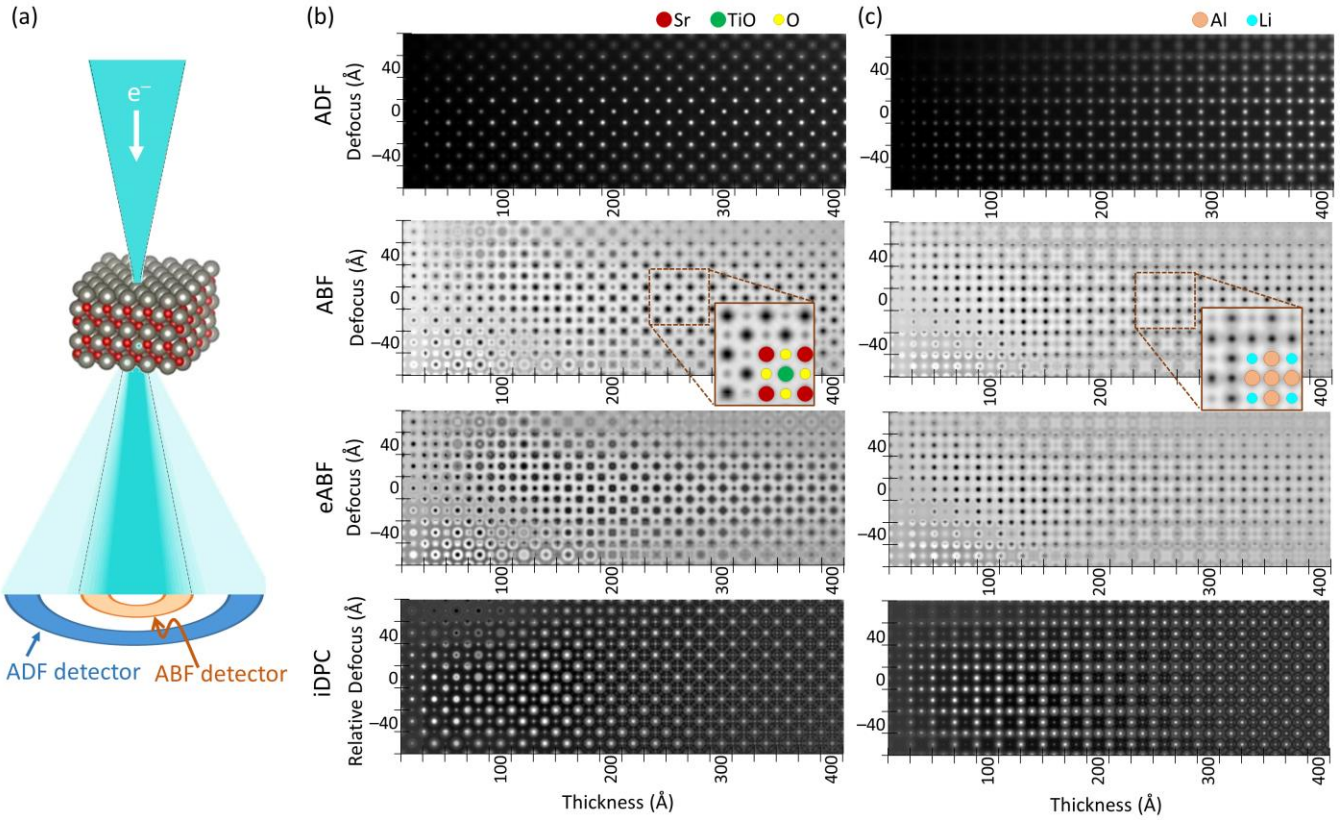

Figure 1. (a) Schematic of STEM experiment showing two annular detectors (for ADF and ABF) in the diffraction plane. (b) Thickness-defocus tableaus for ADF, ABF, eABF and iDPC of $SrTiO_3$ [001] simulated using an absorptive model. Accelerating voltage = 200 kV, probe-forming aperture semiangle = 23 mrad, HAADF detector range = 81–228 mrad, ABF detector range = 11.5–23 mrad. Whereas the ADF, ABF and eABF tableaus are given with defocus relative to the sample entrance surface, in the case of iDPC the defocus is given relative to the specimen mid-plane. (c) As for (b) but for Al_3Li [001].

doi:10.1017/S1431927619003295
Microsc. Microanal. 25 (Suppl 2), 2019

Advances in STEM and EELS: New Operation Modes, Detectors and Software

A.L. Bleloch[1], N.J. Bacon[1], G.J. Corbin[1], N. Dellby[1], M.V. Hoffman[1], M.T. Hotz[1], P. Hrncirik[1], N. Johnson[1], T.C. Lovejoy[1], C.E. Meyer[1], A. Mittelberger[1], B. Plotkin-Swing[1], G.S. Skone[1], Z.S. Szilagyi, and O.L. Krivanek[1,2] *

[1.] Nion R&D, 11511 NE 118th St, Kirkland, WA, 98034, USA
[2.] Department of Physics, Arizona State University, Tempe AZ 85287, USA
* Corresponding author: krivanek@nion.com

Advances in the capabilities of scanning transmission electron microscopes (STEMs) and electron energy loss spectrometers (EELS) over the last 2 decades have been remarkable. Modern-day monochromated, aberration corrected STEMs (MAC-STEMs) can give probe sizes of 1.1 Å at 30 kV operating voltage [1], EELS energy resolution of 4.2 meV also at 30 kV [2], and spatial resolution of ~0.3 Å through the use of 4D STEM and ptychographic reconstruction [3]. These achievements have been made possible by aberration correction, and by developments in monochromator, spectrometer and detector design. The electron-optical developments are now maturing, and further improvements in this area are likely to be more incremental. Here we summarize our work on endowing Nion electron microscopes with new capabilities via new operation modes, detectors and software.

One potentially transformative new capability is to map vibrational properties of materials in reciprocal space, i.e. to map the momentum-dependence of vibrational losses [4]. The needed data set is similar to the *(X, Y, ΔE)* energy loss data cube familiar from spectrum-imaging, but with the two spatial coordinates replaced by scattering angles θ_x and θ_y, typically rescaled into momentum space $q = 2\pi\,\boldsymbol{\theta}\,/\lambda$. It promises to give similar information on phonon modes in solids as has been traditionally provided by neutron scattering [5] and more recently inelastic X-ray scattering, but from much smaller volumes. However, the signal is weak, for two reasons: a) the cross-sections are small, and b) when monochromating for 5-10 meV energy resolution, the electron beam current is typically only 3-15 pA.

Hage et al. [4] acquired ω–q line profiles (aka "ω–q diagrams") through the data cube serially, by defining the scattering angles accepted by the EEL spectrometer with a small entrance aperture and shifting the diffraction pattern over the aperture. This method is flexible but inefficient, resulting in acquisition times of tens of minutes or even hours per ω–q diagram. A more efficient collection method consists of placing a slot aperture in the spectrometer entrance plane, and adjusting a diffraction pattern projected onto the slot to encompass the momentum range of interest [6]. Fig. 1 shows an ω–q diagram obtained in this way along the Γ–>M line in h-BN. The diffraction pattern was rotated using the microscope's post-sample lenses to project the desired Brillouin zone line onto the slot aperture, 125 µm wide and 2 mm long, and the data was summed over 30 acquisitions of 10 seconds each. The information is equivalent to Fig. 2 of [6], but the acquisition time was much shorter – about 5 minutes.

Acquiring ω–q data as above places high demands on the EELS detector. It needs to give a wide dynamic range (10^5:1 and higher), narrow point spread function (PSF) so that the high intensity of strong Bragg discs does not "spill" into the much weaker signal at ΔE>0, q>0 immediately next to the discs, and ideally single-electron sensitivity. The detector used to record the data for Fig. 1 was an ultra-low noise SCMOS camera lens-coupled to a P43 scintillator. Its main strength lies in combining high speed (400 Mpixels / second, i.e. 100 2kx2k frames per second, or 1000 EEL spectra of 2048x200 pixels

per second) with ultra-low noise (1.6 well e^- r.m.s.) read-out. However, it only gives detective quantum efficiency (DQE) >0.5 with about five 30 keV electrons per pixel, i.e. it is not able to detect single 30 keV electrons. Larger-pixel, fiber-optically coupled SCMOS cameras are able to detect single electrons, but their read-out is ~5x slower, and hence not as well optimized for fast elemental mapping.

The best detector for ω–q diagrams and other EELS applications at 30-200 keV primary energy is likely to be a directly illuminated hybrid pixel detector, with single electron sensitivity and high read-out speed. Fig. 2. shows a core loss spectrum of h-BN recorded on a prototype of such a detector that uses a single Medipix3 chip. The spectrum comprises the zero loss peak (ZLP), BN plasmon and B K-edge, all recorded in the single electron detection mode, with DQE ~ 0.8. The PSF is much better than for scintillator-based cameras: only about 1.2 pixels wide, and the drop-off of the intensity on the energy gain side is especially impressive: down to $2x10^{-5}$ within 3 pixels. In order to avoid saturation, the current in the ZLP was set to a low value of 0.7 pA and spread over 16 pixels in the non-dispersion direction. Had the ZLP been spread sideways to cover the full 256 pixel width of the sensor, a ZLP current of 11 pA could have been recorded, but this value is still too low for many practical applications. We are therefore developing a larger-format direct detection camera for EELS applications whose saturation threshold is about 10x higher, and expect to report on it at the meeting.

Other developments we intend to review at the meeting include testing the Nion microscope's ability to protect its cold field emission gun (CFEG) in the presence of large gas pressures at a sample in an aperture-type environmental gas cell, which showed that pressures up to ~10 torr at the sample are feasible with appropriate differential pumping; and new software developments, especially in the areas of probe, monochromator and spectrometer autotuning.

[1] O.L. Krivanek et al., Microsc. Microanal. **24** (Suppl 1, 2018), 18.
[2] O.L. Krivanek et al., Ultramicroscopy (2019) in press, doi.org/10.1016/j.ultramic.2018.12.006
[3] Y. Jiang et al., Nature **559** (2018) 343-349, doi.org/10.1038/s41586-018-0298-5.
[4] F.S. Hage et al., Sci. Adv. 2018;4:eaar7495 1-5.
[5] P.C.H. Mitchell et al., Vibrational Spectroscopy With Neutrons, World Scientific (2005).
[6] G. Mollenstedt, Optik **5**, 499 (1949).

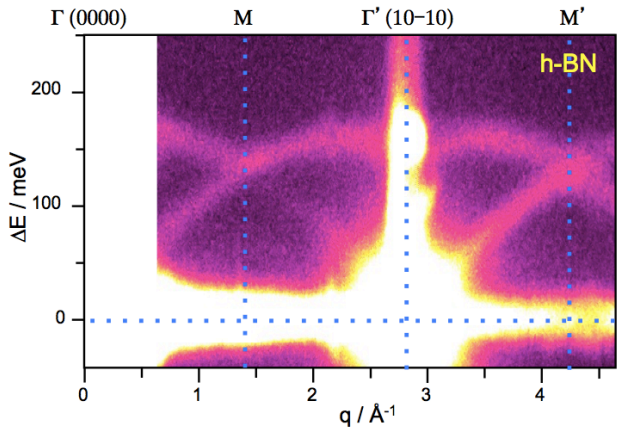

Figure 1. Experimental ω–q diagram of BN along the Γ–M line, recorded in parallel in 300 sec. Nion HERMES, 30 keV. Saturation was minimized by excluding the Γ point from the slot aperture.

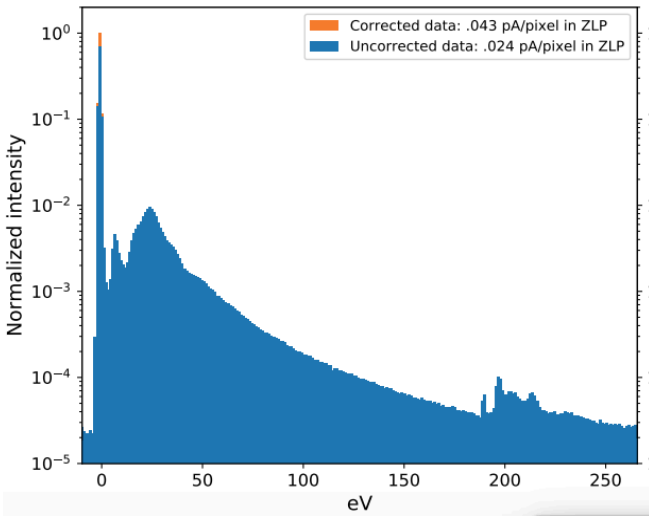

Figure 2. EELS of BN acquired with a Medipix 3 256x256 hybrid pixel detector. 30 keV, 20,000 x 0.5 ms exposures (total exposure 10 s).

Ptychographic Scanning-TEM imaging by JEOL:

1. **Fast Pixelated Detectors: A New Era for STEM, JEOL News Vol. 53 No. 1** *(Peter D. Nellist)*

Fast Pixelated Detectors: A New Era for STEM

Summary **Information**

JEOL NEWS Vol.53 No.1

Peter D Nellist and Gerardo T Martinez

Department of Materials, University of Oxford

Conventional detectors for the scanning transmission electron microscope (STEM), such as the annular dark-field or annular bright-field detectors, integrate the intensity in the detector plane of the STEM over a range of scattering angles. In doing so, they neglect the rich information present in the intensity variations in the detector plane. Here we demonstrate that a recently developed fast pixelated detector, the JEOL 4DCanvas™ system, now allows the routine recording of the full four-dimensional STEM imaging data set. The four dimensions consist of the two real-space coordinates corresponding to the illuminating probe position, and the two reciprocal-space coordinates corresponding to position in the detector plane. Because the STEM probe pixel dwell time is now limited by the frame speed of the camera, one of the key developments is high frame rates of greater than 1000 frames per second. A second key development is direct electron detection with single electron sensitivity. We show that the 4D data set can be used to synthesize a range of STEM imaging modes from a single scan. We go on to use ptychography to retrieve the phase shift of the transmitted beam, showing how efficient phase imaging can now be achieved in STEM. It is shown that aberration correction is possible post-acquisition, and we explore the effects of dynamical scattering from heavier samples.

Introduction

Over the past two decades, the scanning transmission electron microscope (STEM) has become the instrument of choice for atomic resolution imaging and spectroscopy studies of materials, especially where quantitative information is required. There are two main reasons for this: (i)

STEM allows for simultaneous imaging and spectroscopy revealing structure, composition and bonding at atomic resolution. (ii) The commonly-used imaging STEM modes are incoherent which leads to easier interpretation of the data [1]. The most commonly-used imaging mode makes use of an annular dark-field (ADF) detector to detect the intensity of the scattering to relatively high angles. The resulting ADF images show both an incoherent nature and compositional sensitivity and are therefore are a very powerful way of imaging materials [2]. In ADF STEM imaging, the total intensity incident upon the entire ADF detector is summed to give a value for the image pixel corresponding to the probe position. Any detail or variation of intensity in the STEM detector plane within the collection area of the detector is therefore lost. In this paper we explore how such intensity variations can be used in STEM, in particular through the use of ptychography to provide phase imaging.

Before the widespread availability of high-resolution STEM instruments, atomic resolution imaging was performed using phase contrast imaging in a conventional TEM (CTEM), a technique which became referred to as high-resolution TEM (HRTEM) [3]. In such images, dynamical scattering of electrons in the sample and changes in the precise imaging parameters can strongly affect the image, including leading to contrast reversals where it is not immediately clear whether the atoms or atomic columns appear as dark or bright contrast (see for example [4]). In contrast, the incoherent nature of ADF STEM always leads to bright peaks for atoms or atomic columns. Samples, such as graphene, that are thin and contain light elements are much more efficiently imaged in HRTEM compared to ADF STEM because the electron scattering from such samples can be regarded as only producing a small phase shift in the transmitted electron wave. It can be shown that weak phase objects produce very little signal in ADF STEM [5], whereas in the CTEM aberrations can be used to form a virtual phase plate that allow weak phase contrast imaging. The importance of phase contrast imaging in the CTEM has been highlighted in the biological imaging field by the award of the 2017 Nobel Prize in Chemistry for the development of cryo-EM. The imaging used for single particle analysis in biological imaging is phase contrast imaging, and indeed this has been the driver for the development of phase plates to enhance the phase contrast [6].

By the principle of reciprocity [7, 8], the configuration of the STEM detector plays the same role as the illumination configuration in a CTEM. As shown in Fig. 1, a small, axial bright-field (BF) detector in STEM is equivalent to highly parallel, axial illumination in the CTEM. A larger STEM detector is equivalent to a more highly convergent incoherent beam in the CTEM. The ADF detector in STEM is somewhat similar to hollow-cone illumination in CTEM. For HRTEM phase contrast imaging, a highly parallel, high-coherence beam is required, which is equivalent to the small axial STEM detector. It is now clear why the CTEM is more efficient than the STEM for HRTEM work: in the CTEM, a parallel beam illuminates the sample, and the scattering up to some

angle corresponding to the numerical aperture of the lens is collected and imaged with the majority of the scattered electrons being detected. In the STEM, a highly convergent beam illuminates the sample but only electrons transmitted to a small axial detector are collected, so only a small minority of the transmitted electrons are detected. For radiation-sensitive materials where the efficiency of the imaging process is crucial, BF STEM imaging is not optimal.

In this paper we consider a fast pixelated detector (FPD) that records a two-dimensional intensity map of the STEM detector plane for each probe position in a two-dimensional scan, resulting in a four-dimensional (4D) data-set that can be regarded as the universal STEM imaging data set. We show that the 4D data set allows quantitative phase imaging, and because all the transmitted electrons are detected is very electron-efficient allowing relatively low-dose imaging.

Fig. 1

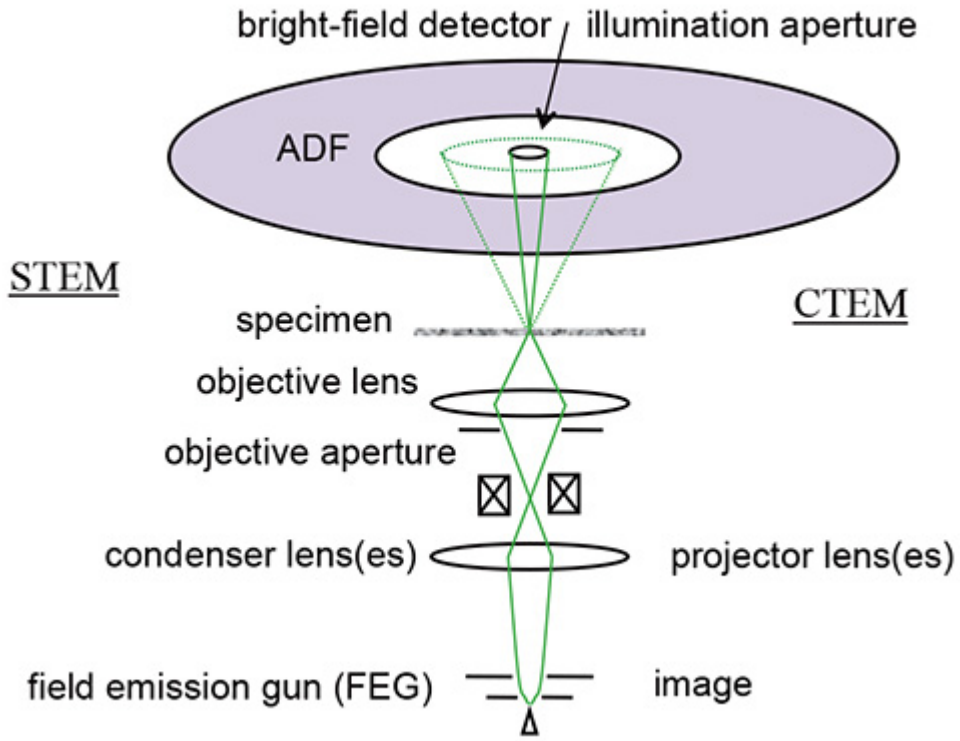

A comparison of the imaging configuration for phase contrast imaging in the CTEM and the STEM demonstrating the principle of reciprocity. In the CTEM, a small illuminating aperture is used to provide close to parallel illumination. The convergence angle of the beam is much smaller than the acceptance angle (numerical aperture) of the objective lens. All the unscattered and much of the scattered electrons are therefore detected. By reciprocity, the equivalent for STEM is a small bright-field detector that is much smaller than the unscattered, bright-field disc in the detector plane. Much of the unscattered and scattered electrons are therefore not detected, and is therefore not an efficient use of electrons.

Experimental Details

When recording the 4D STEM data set, the probe pixel dwell time in the scan is limited by the frame-speed of the detector. Typical STEM dwell times are less than 100 µs, and so detectors with extremely high frame rates are required. The detector should also offer single electron sensitivity with a high detector quantum efficiency. The work presented here was all recorded using a JEOL 4DCanvas™ system [9] mounted on a JEOL JEM-ARM200F cold field emission STEM system fitted with a probe optics aberration corrector. The 4DCanvas™ is a highly sensitive multi-channel STEM detector with channels of dimension 264 × 264. It can be read out at a speed of 1,000 frames per second (fps), or commensurately faster with binning (for example 4 by 1 binning gives 4,000 fps). The sensor of this pixelated detector is a direct electron detection charge coupled device. The Oxford system is shown in Fig. 2.

Fig. 2

A photograph of the JEOL JEM-ARM200F instrument at the Department of Materials in Oxford along with a photograph of the JEOL 4DCanvas™ system as fitted to the microscope.

Results

Synthesis of conventional STEM images

We start by considering the imaging of the edge of a sample of Pt prepared by focused ion-beam lift-out and oriented along the <110> direction. A 4D data set was recorded at a beam energy of 200 keV from a 512 by 512 probe scan area with the detector operating without binning at 1,000 fps. Figure 3a shows a single detector image frame. The single electron detection is clear in the

image. Summing over all probe positions to give a position-averaged convergent beam electron diffraction pattern (PACBED)(Figures 3b and 3c) shows the usual form of a convergent beam electron diffraction pattern.

From this data set, images from a range of different STEM detectors can be synthesized. This is achieved by integrating the 4D data set over the desired detector geometry in the detector plane of the data, resulting in a 2D image. Figure 4 shows the images from the incoherent bright field (IBF), annular bright-field (ABF), annular dark-field (ADF) and low-angle annular dark-field (LAADF) geometries with their integration regions displayed using the PACBED intensities. In particular it can be seen how the LAADF image shows a "halo" type contrast. This can be explained by considering that the LAADF intensity will maximize when the BF disc is at its maximum deflection, which will occur when the probe is slightly displaced from the centre of an atomic column and the illuminating electrons are experiencing the maximum net electric field, similar to the effect seen for differential phase contrast imaging [10] and similar to the effect seen for first-moment imaging [11].

Fig. 3

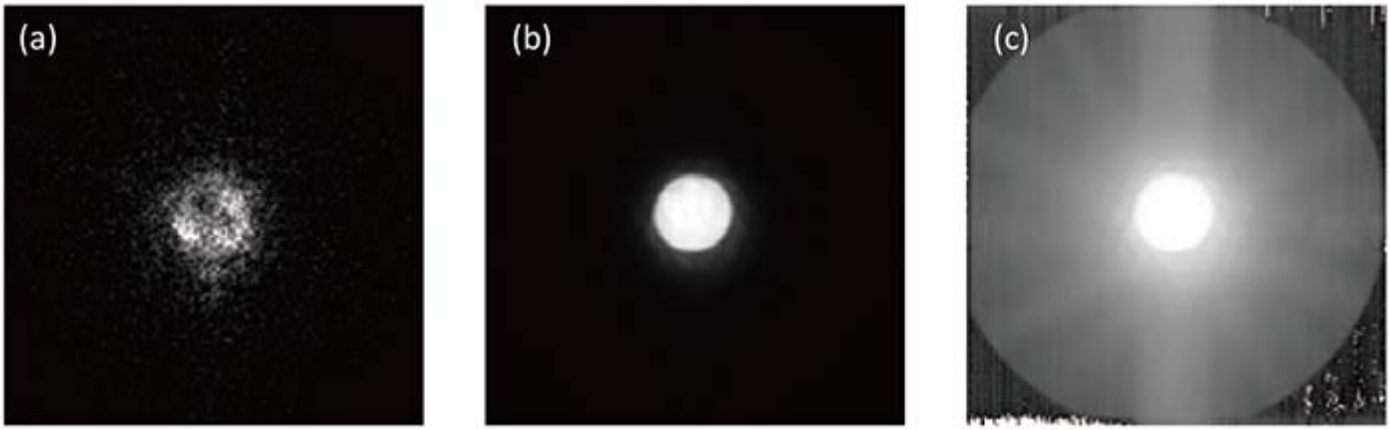

Data recorded from the 4DCanvasTM system during a 512 by 512 probe position scan over a sample of Pt <110> with the camera operating in full-frame mode at 1,000 fps. (a) A single frame where the bright points of intensity represent single electrons being detected. (b) The sum of diffraction patterns from the entire scanned area to form a position averaged CBED (PACBED) pattern.(c) The logarithm of the intensity of the PACBED pattern so that the Kikuchi lines are visible. The shadow of the JEOL ADF1 detector is also visible.

Fig. 4

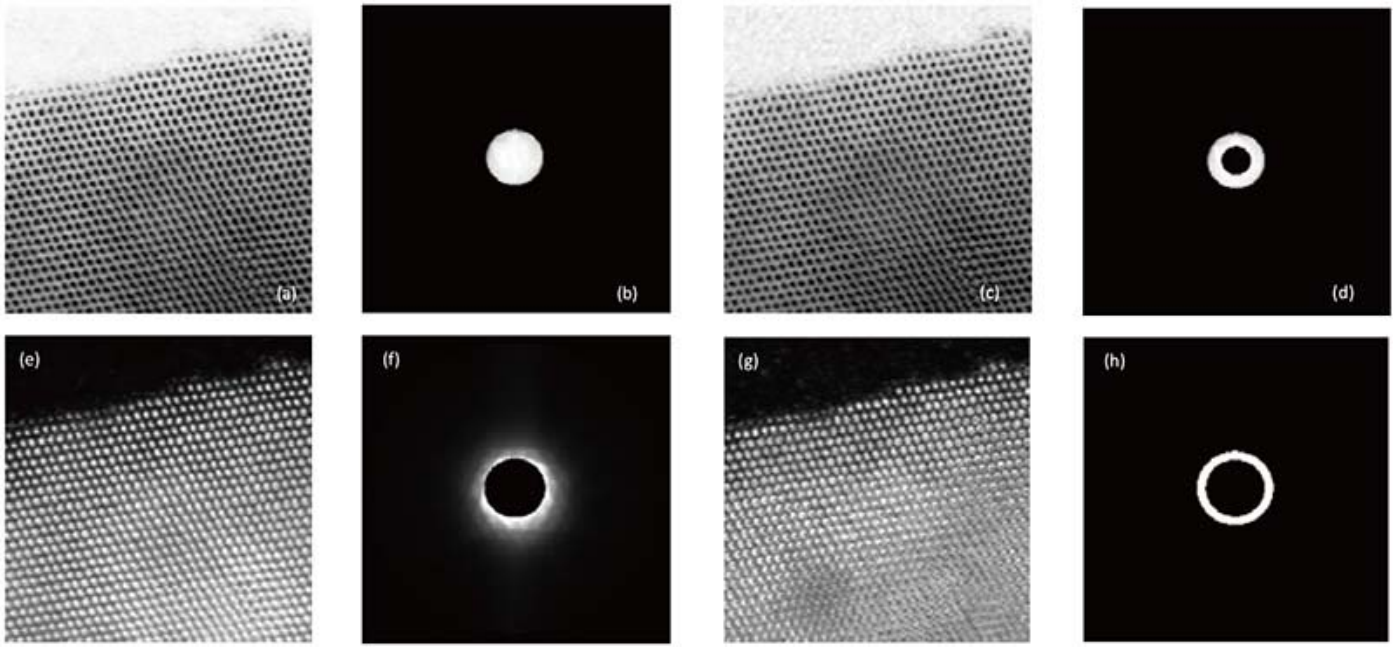

Synthesised STEM images from the data recorded in Fig. 3. (a), (c), (e) and (g) show images for IBF, ABF, ADF and LAADF respectively, with the integration regions over the detector illustrated in (b)(d)(f)(h) respectively.

Phase imaging through ptychography

In addition to allowing a flexible choice of imaging detector geometries that can be selected post-acquisition, the 4D data set creates a range of opportunities for new imaging modes that are only just starting to be explored. One such new mode is phase imaging through electron ptychography. Ptychography was proposed by Hoppe [12] as a method to solve the phase problem in electron diffraction, and was demonstrated experimentally in the early 1990s in the context of focused-probe STEM by Rodenburg and co-workers [13, 14]. At that time, camera and computing technical capabilities severely limited the technique, and images with typically only 32 by 32 pixels were achieved. The development of FPDs has enabled ptychography to become a viable and powerful technique in STEM. The 4DCanvasTM system installed on a JEM-ARM200F STEM at Oxford was the instrumentation on which ptychography was first used to solve the previously unknown structure of a recently synthesized material [15].

As described in [15], ptychography makes use of overlapping discs in a coherent convergent beam electron diffraction pattern. In the STEM configuration, the sample is illuminated by a highly convergent beam that is focused to form the probe. For a crystalline sample, the diffracted beams will form discs in the STEM detector plane, and in the overlap between these discs, coherent interference will occur. The resulting intensity will depend on the phase of the diffracted beams, any aberrations in the probe-forming optics, and the probe position. As the probe is scanned, the intensity in the disc overlap regions will fluctuate. Indeed, it is this fluctuation that is the origin of lattice contrast in any STEM image. Assuming the aberrations are corrected to zero, the phase of

this fluctuation with respect to probe position is the phase difference between the interfering diffracted beams. From this information, the phases of all the beams can be determined. Once the phase problem is solved, it no longer makes sense to describe a method as being imaging or diffraction since the data can be readily converted from one to the other through a Fourier transform. Ptychography is thus a combination of diffraction and imaging.

It should be noted that the ptychography method implemented here for focused-probe STEM is not limited to perfect crystals, but is general to any object as long as the transmission by the sample can be modelled as a multiplicative transmission function. The mathematical approach used is described in more detail in [16] and modified for the current work as described in [15], but for completeness we describe it briefly here. The 4D measured data set is denoted $|\boldsymbol{M}(\boldsymbol{Kf}, \boldsymbol{R_o})|^2$ where the position in the detector plane is given by the reciprocal space vector $\boldsymbol{Kf}$ and the illuminating probe position by $\boldsymbol{R_o}$. Taking the Fourier transform of the data set with respect to the $\boldsymbol{R_o}$ coordinate, but not the $\boldsymbol{K_f}$ coordinate gives

$$\boldsymbol{G(K_f,Q_p) = A(K_f)A^*(K_f + Qp) \otimes_{K_f} \psi(K_f)\psi^*(K_f - Q_p)}$$

where $\boldsymbol{Q_p}$ is the image spatial frequency variable conjugate to $\boldsymbol{R_o}$, $\boldsymbol{A(K)}$ is the aperture function for the illumination with a modulus controlled by the size and position of the objective aperture and phase reflecting any aberrations present, $\boldsymbol{\psi(K)}$ is the Fourier transform of the specimen transmission function, and $\otimes_{\boldsymbol{K_f}}$ denotes a convolution with respect to the detector plane position variable. If $\boldsymbol{A(K)}$ is known, then the product to the left of the convolution can be deconvolved, and the specimen transmission function determined from the product on the right. Thus the amplitude and phase of the specimen transmission function are determined, and both can be plotted fully quantitatively. Given the discussion in the introduction, it is important to note that the phase can be determined quantitatively even if there are no aberrations present. Efficient quantitative phase imaging is possible without the need for a phase plate using STEM ptychography. Figure 5 shows a comparison of images from the same sample taken using a JEOL JEM-3000F instrument running as an HRTEM and a ptychography image from a STEM showing that HRTEM-like imaging is now fully available in STEM.

Fig. 5

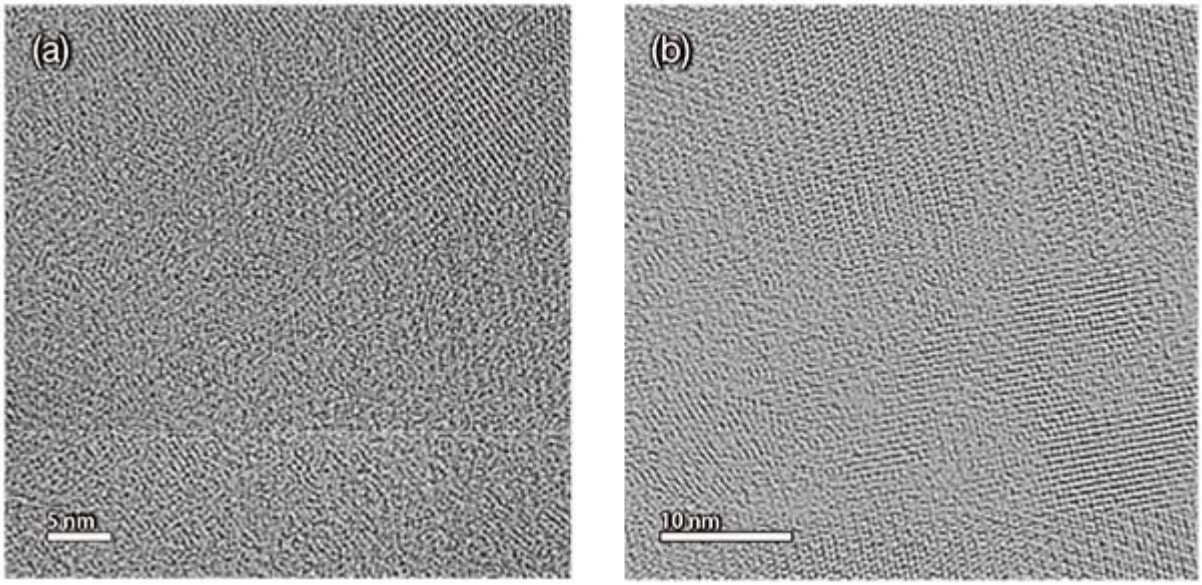

Images of a thin film of a C60/C70 mixture: (a) recorded in a JEOL JEM-3000F instrument running in a CTEM configuration at 300 kV accelerating voltage; (b) recorded in a JEOL JEM-ARM200F instrument running at 200 kV using the 4DCanvas™ detector followed by ptychographic reconstruction. Note the similarity in the contrast revealed using the two types of imaging.

Enabling low-dose imaging

Because all the transmitted electrons are detected when using an FPD, we might expect to form images with much lower noise that was possible with non-segmented detectors, and thus to be able to lower the electron dose while still maintaining sufficient signal to noise in the image. Equation (1) also allows us to know exactly where in the detector plane the information is arising for each spatial frequency in the image, and therefore by just using those regions, the noise (which is distributed across the entire detector plane) is somewhat rejected. It is like having a STEM detector that is adapting itself to be optimal for each different spatial frequency in the image. Figure 6 shows a comparison of imaging using ADF and ptychographic STEM recorded simultaneously of a monolayer of hexagonal boron nitride. In the ptychographic image the noise is very low, and the location of a boron vacancy can be readily identified.

Fig. 6

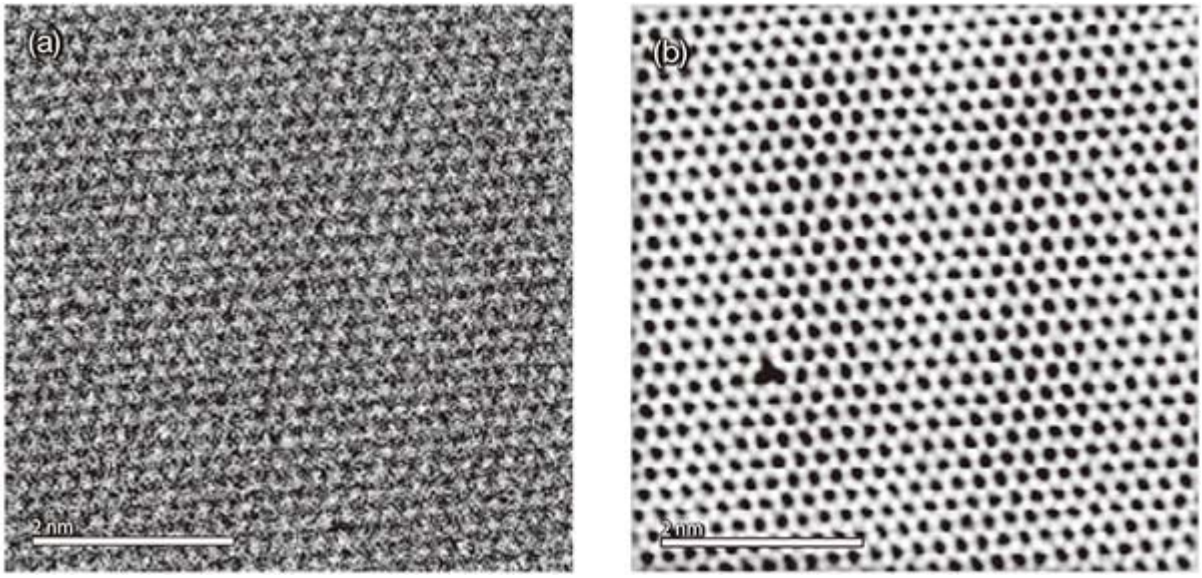

An ADF image and a ptychographic image of hexagonal boron nitride recorded simultaneously at a beam energy of 60 keV. The ptychography image can be seen to be much lower in noise, and a boron vacancy defect can be readily identified.

Aberration correction

Prior to the development of hardware to correct for the aberrations in the electron microscope, it was envisaged that ptychography would offer a solution to the problem of spherical aberration. Once the complex transmission function is known, the effects of aberrations can be deconvolved. This aim for ptychography was overtaken by the successful development of aberration correctors. Nonetheless, it remains the case that often, perhaps because of small aberration drift or imperfect corrector tuning, some residual aberrations remain. The more recently developed iterative methods for ptychography make no initial assumptions about the aperture which is then solved during the iterative process [17]. The direct method used for the results here, does require the aperture function to be known, but it has also been shown that in the case of a weak-phase object the residual aberrations can be directly measured from the function given in Equation (1), and then can be deconvolved [15]. Figure 7 shows that even for a substantially misaligned instrument the aberration correction offered by ptychography is able to recover an image correctly reflecting the structure of the sample.

An additional benefit arising from the ability to correct aberrations is that a reconstruction can be performed assuming a specific defocus. It has been shown that this approach allows for an optical sectioning effect leading to three-dimensional reconstructions of the object [15]. The 3D information is inherently stored in the 4D data set recorded from the microscope even though the data has been recorded from a single scan at a fixed defocus.

Fig. 7

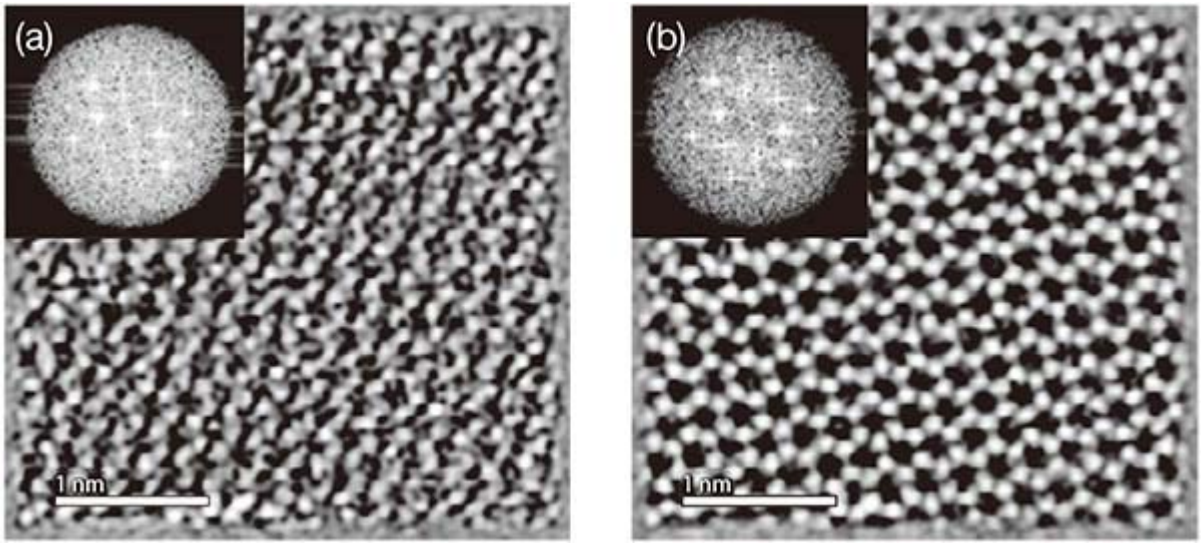

(a) An image of graphene recorded at 80 kV with the microscope misaligned leading to large residual aberrations. (b) From the ptychographic data set, the aberrations have been measured and corrected so that the lattice is now visible. The Fourier transform of the images show that the second ring of spots are all now visible, unlike the Fourier transform of image (a).

Dynamical effects

The theoretical basis for ptychography described above assumes that the interaction of the electron beam with the sample can be described by a multiplicative transmission function. For thicker and heavier samples, dynamical electron scattering conditions apply, and in this case the multiplicative approximation cannot be made. In the multiplicative approximation, it is assumed that the amplitude or phase of a diffraction beam is not dependent on the angle of the incoming beam with respect to the sample. In the case of dynamical scattering, there is a dependence. Nonetheless, there is nothing to stop the 4D data set being recorded, and we can apply the same ptychographic reconstruction method to the data. Returning to the Pt wedge sample used in the data for Fig. 4, we can now perform a ptychographic reconstruction, as shown in Fig. 8. The peaks in the phase image can still be seen to be localized to the atomic column positions and there are no contrast reversals visible. At some thicknesses, the peaks show a "halo"-like structure. Similar results have been shown by Yang et al. [18]. Although a more detailed study is required, it appears that the ptychographically reconstructed phase images are more robust to dynamical effects and thickness changes than HRTEM images.

Fig. 8

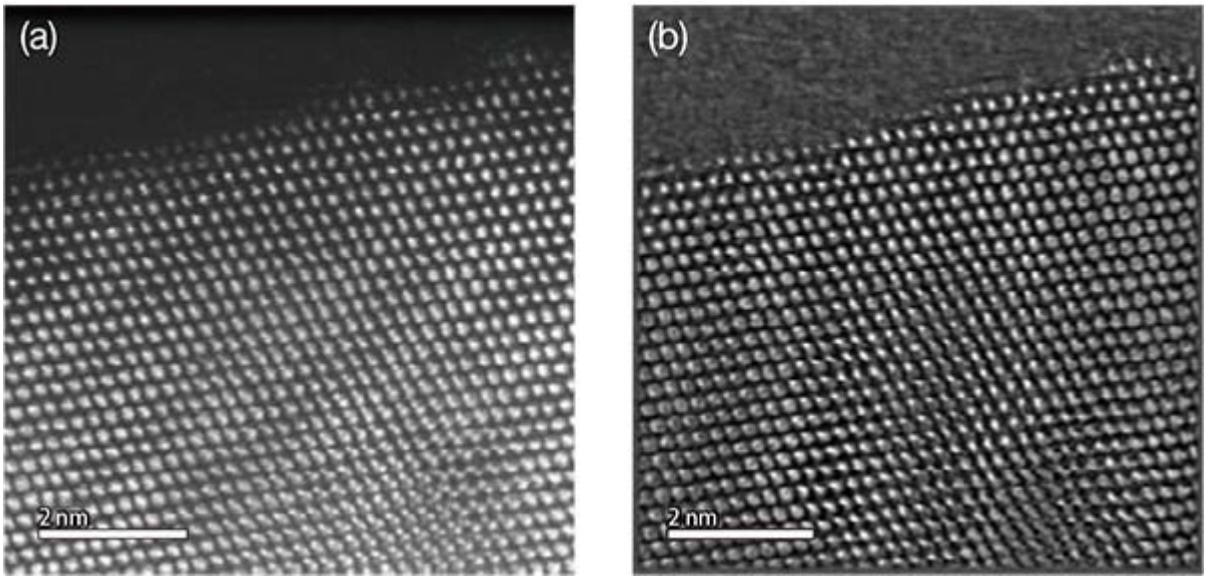

The ADF image (a) and the ptychographic phase image (b) from the Pt wedge sample also used in Fig. 4. As the thickness increases, the phase image starts to form "halo" like contrast, but the peak is still located at the atomic column position and contrast reversals are not seen. Note that there is an inclined stacking fault towards the lower right of the image so additional atomic columns are visible.

Conclusion

The development of FPDs for STEM has allowed for highly flexible imaging in STEM and has created opportunities for new imaging modes. Here we have explored applications of electron ptychography, and shown how focused probe electron ptychography can be performed alongside conventional STEM modes such as ADF. The resulting phase image bears many similarities to HRTEM, but is also seen to have a very high signal-to-noise ratio and is robust to dynamical effects. Ptychography also allows for the correction of residual aberrations which further improves image contrast and allows for optical sectioning for 3D imaging.

Although STEM has become the preeminent instrument for atomic resolution studies, HRTEM has remained popular for light and thin samples, such as graphene and other layered materials, and of course is the main mode for cryo-EM of biological structures. Given that it has now been demonstrated that ptychography in STEM can deliver low-noise phase images, alongside all the other benefits of STEM, it may be that we are on the cusp of a paradigm shift where STEM becomes regarded as a powerful phase imaging instrument. The development of FPDs for STEM now allow fields of view comparable with HRTEM, and Figure 9 shows a 1k by 1k scanned image.

Finally, we note that ptychography is just one new mode possible with an FPD detector. Other authors have explored possibilities associated with measuring the angular dependence of the scattering at higher angles. Methods such as transmission Kikuchi diffraction become available,

and using lower convergence angles the strength of all available diffraction spots can be measured as a function of probe position to give multiple diffraction contrast images in parallel, giving much greater information for dislocation burgers vector determination through g.b analysis for example.

Fig. 9

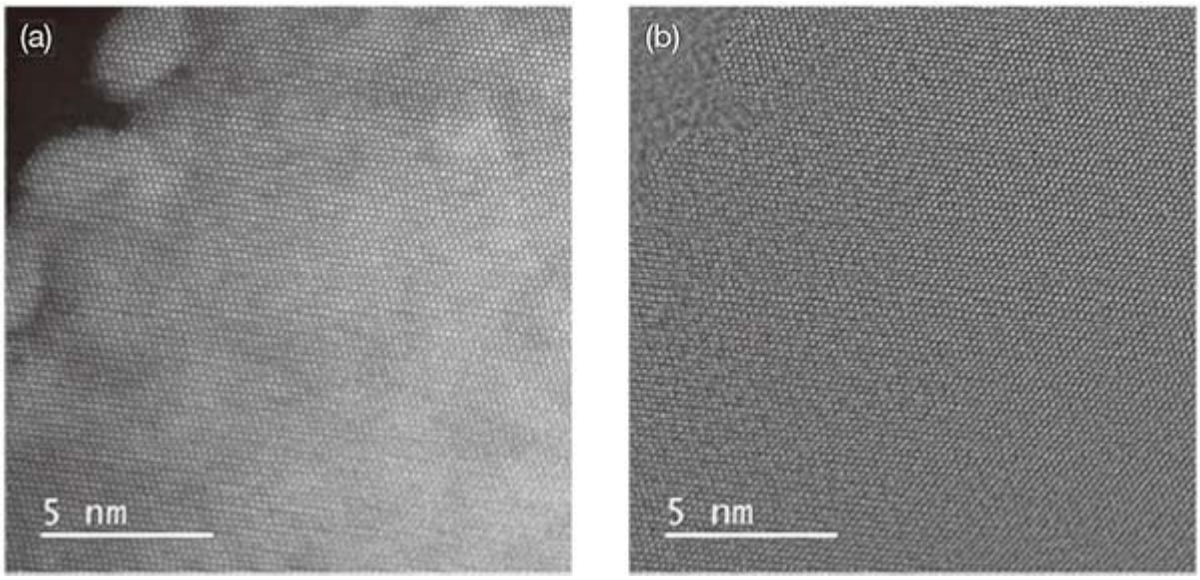

A simultaneously recorded (a) ADF and (b) ptychographic phase image from a Pt <110> wedge sample with 1 k by 1 k probe sampling recorded with a FPD frame speed of 4,000 frames per second demonstrating that large fields of view are possible in focused-probe STEM.

Acknowledgments

We acknowledge the fruitful collaboration with Y Kondo and R Sagawa, JEOL Tokyo, M Simson, M Huth, H Soltau, PNDetector GmbH, and L Strueder PNSensor GmbH, Germany. We also acknowledge experimental assistance from L Jones. Samples have been provided by S Nam and D Bradley (University of Oxford), Y Sasaki (Japan Fine Ceramics Centre), A Béché and D Batuk (University of Antwerp). Support for this project has been received from the EPSRC (grant number grant EP/M010708/1).

References

1. P. D. Nellist, Scanning Transmission Electron Microscopy, in: *Science of Microscopy* P.W. Hawkes, J. C. H. Spence (Eds.), Springer, 2007, pp. 65-132.
2. P. D. Nellist, S. J. Pennycook, The Principles and Interpretation of Annular Dark-Field Z-Contrast Imaging, Advances in Imaging and Electron Physics, **113** (2000) 148-203.

3. D. J. Smith, The realisation of atomic resolution with the electron microscope, Reports of Progress in Physics, **60** (1997) 1513-1580.
4. R. W. Glaisher, A. E. C. Spargo, D. J. Smith, A Systematic Analysis of HREM Imaging of Elemental Semiconductors, *Ultramicroscopy*, **27** (1989) 35-52.
5. T. J. Pennycook, A. R. Lupini, H. Yang, M. F. Murfitt, L. Jones, P. D. Nellist, Efficient phase contrast imaging in STEM using a pixelated detector. Part 1: Experimental demonstration at atomic resolution, *Ultramicroscopy*, **151** (2015) 160-167.
6. M. Marko, A. Leith, C. Hsieh, R. Danev, Retrofit implementation of Zernike phase plate imaging for cryo-TEM, *Journal of Structural Biology*, **174** (2011) 400-412.
7. J. M. Cowley, Image Contrast in a Transmission Scanning Electron Microscope, *Applied Physics Letters*, **15** (1969) 58-59.
8. E. Zeitler, M. G. R. Thomson, Scanning Transmission Electron Microscopy, *Optik*, **31** (1970) 258-280 & 359-366.
9. https://www.jeol.co.jp/en/news/detail/20170726.2143.html.
0. N. Shibata, S. D. Findlay, Y. Kohno, H. Sawada, Y. Kondo, Y. Ikuhara, Differential phase-contrast microscopy at atomic resolution, *Nature Physics*, **8** (2012) 611-615.
1. K. Müller, F. F. Krause, A. Béché, M. Schowalter, V. Galioit, S. Löffler, J. Verbeeck, J. Zweck, P. Schattschneider, A. Rosenauer, Atomic electric fields revealed by a quantum mechanical approach to electron picodiffraction, *Nature Communications*, **5** (2014) 5653.
2. W. Hoppe, Beugung im Inhomogenen Primärstrahlwellenfeld. I. Prinzip einer Phasenmessung von Elektronenbeugungsinter ferenzen, *Acta Crystalographica **A, 25** (1969) 495-501.*
3. J. M. Rodenburg, B. C. McCallum, P. D. Nellist, Experimental tests on double-resolution coherent imaging via STEM., *Ultramicroscopy*, **48** (1993) 303-314.
4. P. D. Nellist, B. C. McCallum, J. M. Rodenburg, Resolution beyond the 'information limit' in transmission electron microscopy, *Nature*, **374** (1995) 630-632.
5. H. Yang, R. N. Rutte, L. Jones, M. Simson, R. Sagawa, H. Ryll, M. Huth, T. J. Pennycook, M. L. H. Green, H. Soltau, Y. Kondo, B. G. Davis, P. D. Nellist, Simultaneous atomic-resolution electron ptychography and Z-contrast imaging of light and heavy elements in complex nanostructures, *Nature Communications*, **7** (2016) 12532.
6. J. M. Rodenburg, R. H. T. Bates, The Theory of Super-Resolution Electron Microscopy via Wigner-Distribution Deconvolution, Philosophical Transactions of the Royal Society of London **A, 339** (1992) 521-553.
7. A. M. Maiden, J. M. Rodenburg, An improved ptychographical phase retrieval algorithm for diffractive imaging, *Ultramicroscopy*, **109** (2009) 1256-1262.
8. H. Yang, I. MacLaren, L. Jones, G. T. Martinez, M. Simson, M. Huth, H. Ryll, H. Soltau, R. Sagawa, Y. Kondo, C. Ophus, P. Ercius, L. Jin, A. Kovács and P. D. Nellist. Electron

ptychographic phase imaging of light elements in crystalline materials using Wigner distribution deconvolution, *Ultramicroscopy* **180** (2017) 173-179.

Related Products